1

General Introduction

1.1 Introduction

This chapter introduces permanent magnet (PM) synchronous machines (PMSMs), i.e. brushless ac (BLAC) machines and PM brushless dc (BLDC) machines. It also describes the basic principles of BLAC and BLDC drives, including modeling and control techniques. In the literature, PMSMs are often referred to as PM BLAC machines only. In this book, the terminologies of both PM BLAC machines and PMSMs will be used for convenience, but PM BLAC drives will only be used together with PM BLDC drives. Moreover, the term "PM machines" used in this book specifically refers to PM brushless machines. This chapter introduces various rotor position sensorless control techniques, as well as a comprehensive classification and their applications. Finally, the scope of this book will be illustrated.

1.2 Permanent Magnet Machines

Over the last several decades, significant advancements in PM materials, power electronics devices, and microprocessors have played a crucial role in the development of PM brushless machines. PM brushless machines exhibit a range of advantages, including high efficiency, high torque density, high power density, easy maintenance, and excellent control performance. Hence, they have been used for a wide range of applications, including electric vehicles, renewable energy systems, robotics, industrial automation, domestic appliances, aerospace, etc. With continued research and development, it is likely that the performance and

Sensorless Control of Permanent Magnet Synchronous Machine Drives, First Edition.
Zi Qiang Zhu and Xi Meng Wu.

capabilities of PM brushless machines will continue to improve, making them an even more compelling choice for a range of industrial and commercial applications.

1.2.1 Topologies

Within the last few decades, there has been much research into various machine topologies of PMSMs, which can be rotary or linear. Rotary PMSMs can be classified as in Figure 1.1 [1].

As shown in Figure 1.1, from the type of air-gap fields, PM machines can be divided into radial-field, axial-field, transverse-flux, and hybrid-fields machines, respectively. Compared to radial-field PM machines, axial-field and transverse-flux PM machines can have higher torque and power density [2]–[5]. However, complex manufacturing processes restrict their applications. In terms of stator winding configurations, PM machines can be grouped mainly into two categories:

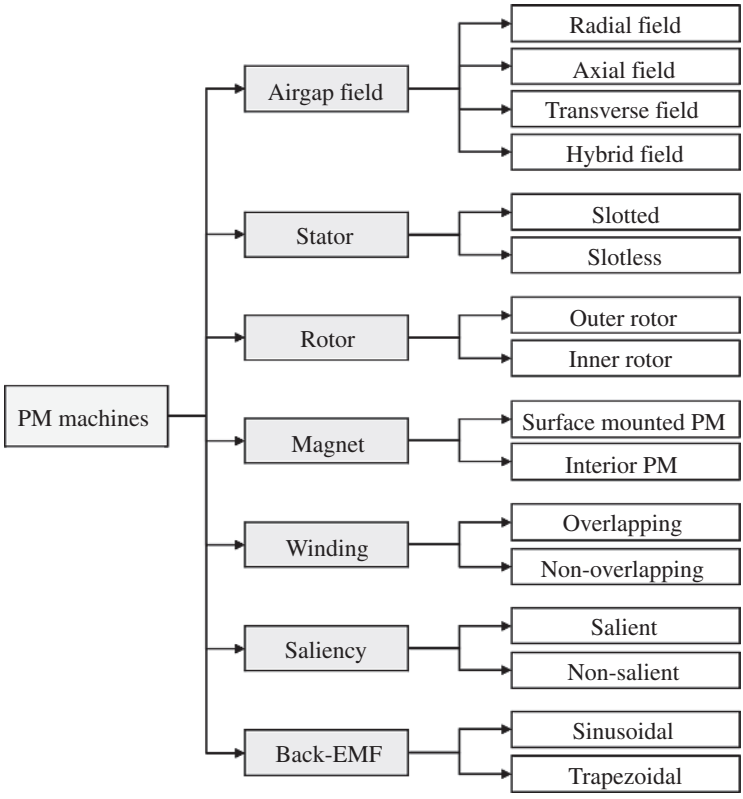

Figure 1.1 Classification of PM machine topologies.

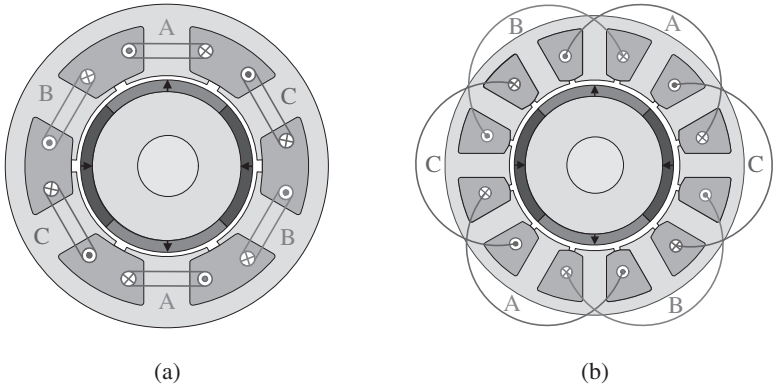

Figure 1.2 Alternate winding configurations for PM machines. (a) Non-overlapping windings. (b) Overlapping windings.

fractional-slot machines with non-overlapping concentrated windings as shown in Figure 1.2a, and integral-slot machines with overlapping distributed windings in Figure 1.2b. Compared to distributed windings, concentrated windings have the advantages of shorter end-windings and a higher slot-packing factor, leading to the reduction of total machine volume, mass, and copper losses [1], [6], [7]. Consequently, the overall efficiency and torque density are improved. However, compared to integral-slot machines, fractional-slot PM machines suffer from high contents of stator magneto-motive force (MMF) harmonics, which could cause increased PM eddy current losses, localized magnetic saturation, acoustic noises and vibrations, etc. [8].

On the other hand, the rotor structures of PM machines can be classified mainly into surface-mounted PM machines (SPM) and interior PM machines (IPM).

As shown in Figure 1.3a, the SPM machine is widely used. It has the advantages of a simple structure and low manufacturing cost. Moreover, the magnet shape can be easily optimized to produce more sinusoidal-distributed flux density in the airgap. However, due to direct exposure to the armature reaction field, the magnets may suffer from irreversible demagnetization risk [1]. In general, the magnets should be retained by a stainless steel sleeve or glass/carbon fiber. Another special SPM machine topology, namely the inset PM machine, is shown in Figure 1.3b, where the magnets are inserted in the rotor with the iron between them. Compared to the SPM machine, the inset PM machine has considerable rotor saliency due to high permeability iron steels between the PMs. Accordingly, it can utilize the reluctance torque to increase the torque density and/or reduce the amount of PM.

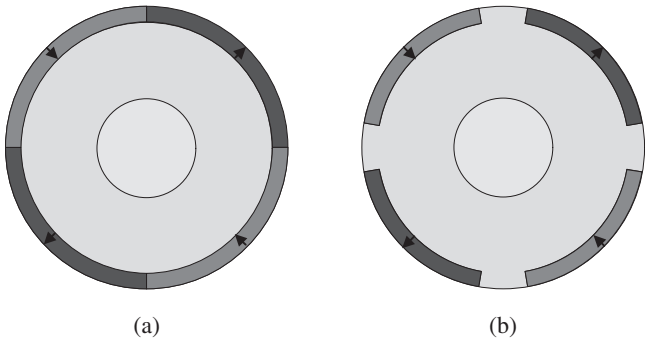

Figure 1.3 Surface-mounted PM rotors. (a) Surface-mounted PM. (b) Surface-inset PM.

In contrast, the IPM structures in which the magnets are placed inside the rotor iron body, shown in Figure 1.4, have the merits of high rotor saliency, good flux-weakening capability, and a low risk of PM demagnetization. According to the rotor PM configurations, the IPM machines can be divided into single-layer IPM rotors, e.g. I-shape and V-shape as shown in Figure 1.4a–b; and double-layer

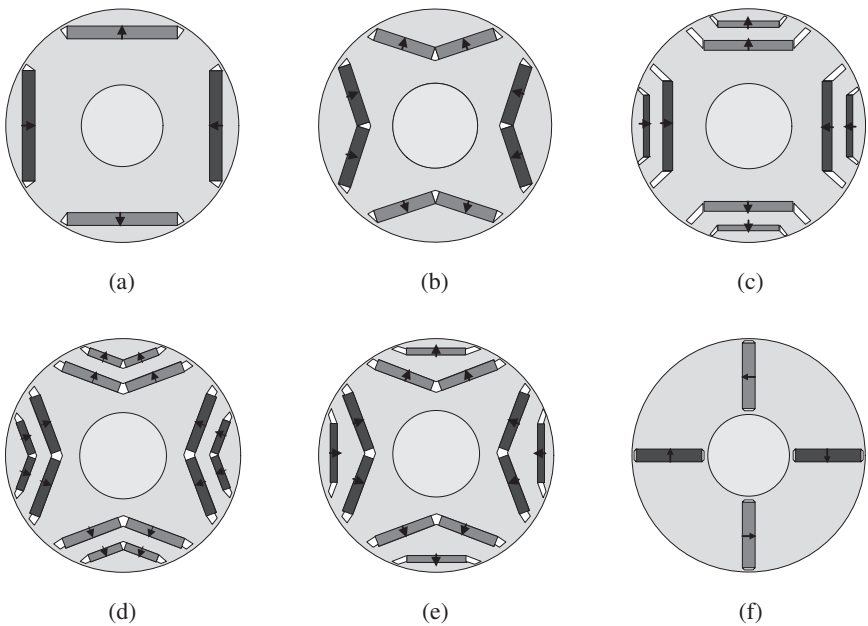

Figure 1.4 Interior PM rotors. (a) Single I-shape PM. (b) Single V-shape PM. (c) Double I-shape PM. (d) Double V-shape PM. (e) Delta-shape PM. (f) Spoke-shape PM.

IPM rotors, e.g. double I-shape, delta-shape, and double V-shape as shown in Figure 1.4c–e; as well as spoke-shape rotors as illustrated in Figure 1.4f, etc.

The I-shape IPM rotor, Figure 1.4a, has a simple construction with rotor saliency. Furthermore, the single-layer V-shape IPM rotor, Figure 1.4b, increases the cross-section areas for PMs and enhances the flux focusing effect, resulting in a better torque capability. For double-layer variants shown in Figure 1.4c–e, i.e. the double I-shape, delta-shape, and double V-shape IPM rotors, the rotor saliency and reluctance torque are further enhanced, but the manufacturing process becomes more complex. In addition, in the spoke-type IPM rotor, Figure 1.4f, the flux focusing effect can be significant if a higher pole number is employed, but a higher leakage flux exists due to additional magnetic bridges near the shaft, and a non-magnetic shaft should be employed and airspace flux barriers are often required in the laminations near the shaft.

1.2.2 Drives

A PM brushless drive consists of a controller, an inverter, and a PM machine, as shown in Figure 1.5. The currents can be measured through three-phase currents, two-phase currents, and dc-link current. The rotor speed and position are usually measured by a position sensor, unless one of the rotor position sensorless techniques is employed, as will be introduced in this book. A voltage sensor is used to measure the dc-link voltage. These feedback signals are sent to the controller, which generates the switching signals for the inverter to achieve the control objective.

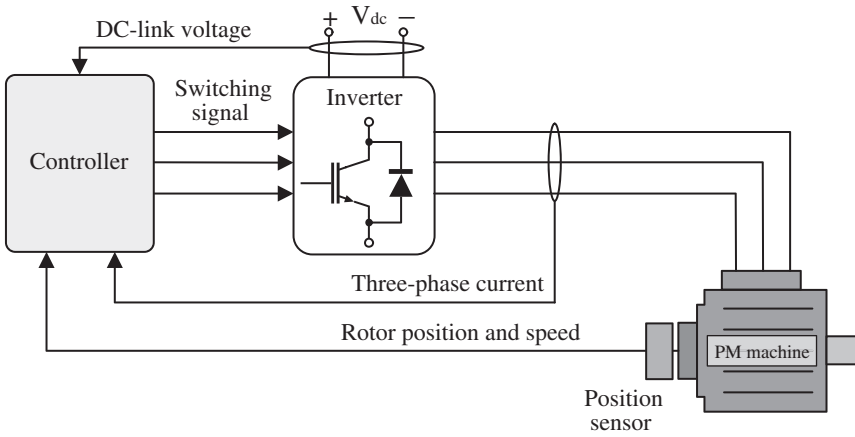

Figure 1.5 Block diagram of a three-phase PMSM drive.

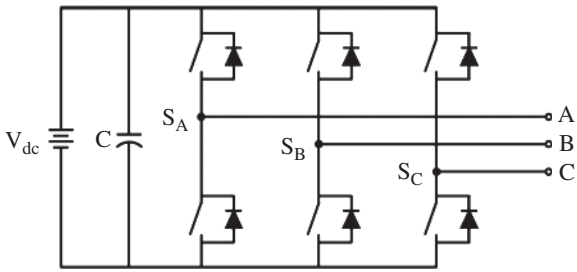

Figure 1.6 Block diagram of a three-phase VSI.

A three-phase voltage source inverter (VSI), Figure 1.6, is commonly employed in a three-phase PM brushless drive system. As shown in Figure 1.6, a VSI consists of six power semiconductor switches, usually IGBTs (insulated gate bipolar transistors) or MOSFETs (metal-oxide-semiconductor field-effect transistors). These six switches form a three-phase bridge, with each leg of the bridge consisting of two switches. The middle point of each leg is connected to the one phase terminal of the PM machine stator winding. The three legs are connected to a dc voltage source with a dc-link capacitor, which is used to smooth the dc-link voltage.

With the rotation of the PM rotor, the back electromotive force (back-EMF) will be generated in the stator windings. The PM machines can be classified according to the back-EMF waveform as either sine-wave or trapezoidal-wave (ideally square-wave), as illustrated in Figure 1.7. The control strategies, which determine the inverter switching status, can be classified as either BLDC or BLAC.

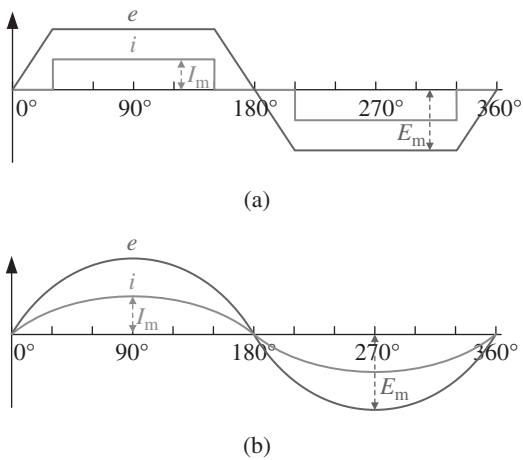

Figure 1.7 Back-EMF waveforms and excitation currents of BLDC and BLAC drives. (a) Trapezoidal back-EMF and square-wave phase current. (b) Sinusoidal back-EMF and sine-wave phase current.

In BLDC operation the inverter ideally supplies square-wave currents, while in BLAC operation the inverter supplies sine-wave currents, as shown in Figure 1.7.

Although both BLAC and BLDC drives use the same VSI, their switching schemes are different. Specifically, BLAC drives employ the three-phase conduction with space vector pulse-width modulation (SVPWM) control to produce the sine-wave current, whereas BLDC drives employ the two-phase conduction six-step control to produce the square-wave current. The switching schemes of BLAC and BLDC drives are described in the following sections.

1.3 Basic Principle of PM BLAC (PMSM) Drives

In this section, the mathematical models and control strategies of BLAC drives [9] are described, providing the reader with a basic understanding of the working principle of PM machine drives. The mathematical models and control strategies of BLDC drives [10], as well as the comparison between BLAC and BLDC drives, will be given in Sections 1.4 and 1.5, respectively.

1.3.1 Modeling

Three-phase PMSMs can be modeled in different reference frames, including the ABC reference frame, stationary reference frame, and synchronous reference frame (which will be shown later in this section). To simplify the modeling, the following assumptions are made:

- The stator winding is distributed symmetrically in space, resulting in a sinusoidal armature reactive MMF.
- The EMF induced in the stator windings by the PM rotor is sinusoidal.
- The three-phase windings are star connected without neutral connection.
- The iron loss and magnetic saturation effect are ignored.
- Parameter changes due to temperature and load are ignored.

1.3.1.1 ABC Reference Frame

In an ABC reference frame, the voltage equation is given by:

$$\begin{bmatrix} v_A \\ v_B \\ v_C \end{bmatrix} = \begin{bmatrix} R_s & 0 & 0 \\ 0 & R_s & 0 \\ 0 & 0 & R_s \end{bmatrix} \cdot \begin{bmatrix} i_A \\ i_B \\ i_C \end{bmatrix} + p \begin{bmatrix} \psi_A \\ \psi_B \\ \psi_C \end{bmatrix} \tag{1.1}$$

where v_A, v_B, v_C are the three-phase voltages, i_A, i_B, i_C are the three-phase currents, e_A, e_B, e_C are the three-phase back-EMFs, ψ_A, ψ_B, ψ_C are the three-phase

flux-linkages. R_s is the phase resistance, and p is the derivative operator, i.e. $p = d/dt$.

The three-phase flux-linkages can be written as:

$$\begin{bmatrix} \psi_A \\ \psi_B \\ \psi_C \end{bmatrix} = \begin{bmatrix} L_{AA} & M_{AB} & M_{AC} \\ M_{BA} & L_{BB} & M_{BC} \\ M_{CA} & M_{CB} & L_{CC} \end{bmatrix} \cdot \begin{bmatrix} i_A \\ i_B \\ i_C \end{bmatrix} + \psi_m \begin{bmatrix} \cos\theta_r \\ \cos(\theta_r - 2\pi/3) \\ \cos(\theta_r + 2\pi/3) \end{bmatrix} \tag{1.2}$$

where L_{AA}, L_{BB}, L_{CC} are the three-phase self-inductances, M_{AB}, M_{BA}, M_{AC}, M_{CA}, M_{BC}, M_{CB} are the three-phase mutual-inductances, ψ_m is the PM flux-linkage, and θ_r is the electrical rotor position. For the inductance matrix, the elements are given by:

$$\begin{aligned} L_{AA} &= L_{s0} - L_{s2}\cos 2\theta_r \\ L_{BB} &= L_{s0} - L_{s2}\cos 2(\theta_r - 2\pi/3) \\ L_{CC} &= L_{s0} - L_{s2}\cos 2(\theta_r + 2\pi/3) \end{aligned} \tag{1.3}$$

where L_{s0} and L_{s2} are the amplitudes of dc and the second order harmonic component of self-inductances, respectively.

$$\begin{aligned} M_{AB} &= M_{BA} = M_{s0} - M_{s2}\cos 2(\theta_r + 2\pi/3) \\ M_{BC} &= M_{CB} = M_{s0} - M_{s2}\cos 2\theta_r \\ M_{CA} &= M_{AC} = M_{s0} - M_{s2}\cos 2(\theta_r - 2\pi/3) \end{aligned} \tag{1.4}$$

where M_{s0} and M_{s2} are the amplitudes of dc and the second order harmonic component of mutual-inductances, respectively. Furthermore, there is no second order harmonic component in the non-salient machines, i.e. $L_{s2} = M_{s2} = 0$.

From (1.1) to (1.4), it can be seen that the machine model in the ABC reference frame is coupled with the rotor position, which makes the control very complex. Therefore, the machine model can be transformed into the stationary reference frame and the synchronous reference frame.

1.3.1.2 Stationary Reference Frame

The machine model can be transformed from the ABC reference frame to the stationary reference frame by using the Clarke transformation, which is given in (1.5).

$$T_{\mathrm{ABC}-\alpha\beta0} = \frac{2}{3}\begin{bmatrix} 1 & -\frac{1}{2} & -\frac{1}{2} \\ 0 & \frac{\sqrt{3}}{2} & -\frac{\sqrt{3}}{2} \\ \frac{1}{2} & \frac{1}{2} & \frac{1}{2} \end{bmatrix}, \quad T_{\alpha\beta0-\mathrm{ABC}} = \begin{bmatrix} 1 & 0 & 1 \\ -\frac{1}{2} & \frac{\sqrt{3}}{2} & 1 \\ -\frac{1}{2} & -\frac{\sqrt{3}}{2} & 1 \end{bmatrix} \tag{1.5}$$

The relationship between the ABC reference frame and the stationary reference frame is shown in Figure 1.8.

Assuming that the three-phase windings are star connected without neutral connection, the sum of the three-phase currents is zero, and the corresponding zero sequence component is zero. After transformation, the voltage and flux-linkage equations in the stationary reference frame are given by:

$$\begin{bmatrix} v_\alpha \\ v_\beta \end{bmatrix} = \begin{bmatrix} R_s & 0 \\ 0 & R_s \end{bmatrix} \cdot \begin{bmatrix} i_\alpha \\ i_\beta \end{bmatrix} + p\begin{bmatrix} \psi_\alpha \\ \psi_\beta \end{bmatrix} \tag{1.6}$$

$$\begin{bmatrix} \psi_\alpha \\ \psi_\beta \end{bmatrix} = \begin{bmatrix} L_{\alpha\alpha} & M_{\alpha\beta} \\ M_{\beta\alpha} & L_{\beta\beta} \end{bmatrix} \cdot \begin{bmatrix} i_\alpha \\ i_\beta \end{bmatrix} + \psi_m \begin{bmatrix} \cos\theta_r \\ \sin\theta_r \end{bmatrix} \tag{1.7}$$

where v_α, v_β, i_α, i_β, ψ_α, and ψ_β are the $\alpha\beta$-axis voltages, currents, and flux-linkages in the stationary reference frame, respectively. $L_{\alpha\alpha}$, $L_{\beta\beta}$, $M_{\alpha\beta}$, and $M_{\beta\alpha}$ are the self- and mutual- inductances in the stationary reference frame, respectively. Furthermore, the inductance elements can be represented as:

$$\begin{aligned} L_{\alpha\alpha} &= \frac{L_d + L_q}{2} + \frac{L_d - L_q}{2}\cos 2\theta_r \\ L_{\beta\beta} &= \frac{L_d + L_q}{2} - \frac{L_d - L_q}{2}\cos 2\theta_r \\ M_{\alpha\beta} &= M_{\beta\alpha} = \frac{L_d - L_q}{2}\cos 2\theta_r \end{aligned} \tag{1.8}$$

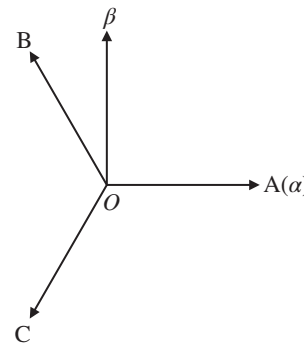

Figure 1.8 Relationship between ABC reference frame and stationary reference frame.

where L_d and L_q are the d- and q-axis inductances. If the machine is non-salient, i.e. SPM, the relationship of the inductances is then given by:

$$L_d = L_q = L_s \tag{1.9}$$

1.3.1.3 Synchronous Reference Frame

The machine model can be transformed from the stationary reference to the synchronous reference frame by using a Park transformation, which is given by:

$$T_{\alpha\beta0-dq0} = \begin{bmatrix} \cos\theta_r & \sin\theta_r & 0 \\ -\sin\theta_r & \cos\theta_r & 0 \\ 0 & 0 & 1 \end{bmatrix} \tag{1.10}$$

$$T_{dq0-\alpha\beta0} = \begin{bmatrix} \cos\theta_r & -\sin\theta_r & 0 \\ \sin\theta_r & \cos\theta_r & 0 \\ 0 & 0 & 1 \end{bmatrix} \tag{1.11}$$

Alternatively, the machine model can be transformed directly from the ABC reference frame to the synchronous reference frame by using a direct-quadrature-zero (DQZ) transformation, which is the product of Clarke transformation and Park transformation. Then, the DQZ transformation matrices are derived as:

$$\begin{aligned} T_{\mathrm{ABC}-dq0} &= T_{\mathrm{abc}-\alpha\beta0} \cdot T_{\alpha\beta0-dq0} \\ &= \frac{2}{3}\begin{bmatrix} \cos\theta_r & \cos(\theta_r - 2\pi/3) & \cos(\theta_r + 2\pi/3) \\ -\sin\theta_r & -\sin(\theta_r - 2\pi/3) & -\sin(\theta_r + 2\pi/3) \\ \frac{1}{2} & \frac{1}{2} & \frac{1}{2} \end{bmatrix} \end{aligned} \tag{1.12}$$

$$T_{dq0-\mathrm{ABC}} = T_{dq0-\alpha\beta0} \cdot T_{\alpha\beta0-\mathrm{ABC}} = \begin{bmatrix} \cos\theta_r & -\sin\theta_r & 1 \\ \cos(\theta_r - 2\pi/3) & -\sin(\theta_r - 2\pi/3) & 1 \\ \cos(\theta_r + 2\pi/3) & -\sin(\theta_r + 2\pi/3) & 1 \end{bmatrix} \tag{1.13}$$

In addition, the relationship between the ABC reference frame, stationary reference frame, and synchronous reference frame is shown in Figure 1.9.

After transformation, by neglecting the zero-sequence component, the voltage and flux-linkage equations in the synchronous reference frame are given by:

$$\begin{bmatrix} v_d \\ v_q \end{bmatrix} = \begin{bmatrix} R_s & 0 \\ 0 & R_s \end{bmatrix} \cdot \begin{bmatrix} i_d \\ i_q \end{bmatrix} + p\begin{bmatrix} \psi_d \\ \psi_q \end{bmatrix} + \omega_r \begin{bmatrix} -\psi_q \\ \psi_d \end{bmatrix} \tag{1.14}$$

and

$$\begin{bmatrix} \psi_d \\ \psi_q \end{bmatrix} = \begin{bmatrix} L_d & 0 \\ 0 & L_q \end{bmatrix} \cdot \begin{bmatrix} i_d \\ i_q \end{bmatrix} + \psi_m \begin{bmatrix} 1 \\ 0 \end{bmatrix} \quad (1.15)$$

where v_d, v_q, i_d, i_q, ψ_d, and ψ_q are the dq-axis voltages, currents, and flux-linkages in the synchronous reference frame, respectively, and ω_r is the electrical rotor speed.

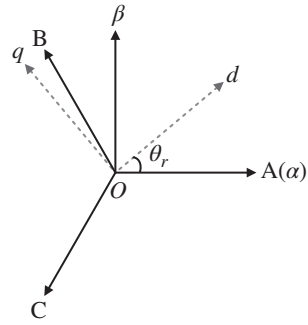

Figure 1.9 Relationship between ABC reference frame and synchronous reference frame.

1.3.2 Control Strategies

As shown in Figure 1.10, it is desirable for the three-phase back-EMFs of a PM BLAC machine to be sinusoidal. Hence, three-phase currents should be controlled to be sine-wave and aligned with or in advance of the back-EMF to maximize the output torque. In order to realize the three-phase sine-wave excitation currents, SVPWM is commonly used to control the VSI to generate the desired stator voltage to the machine. The reference of the stator voltage can be obtained by control strategies, including field-oriented control (FOC), direct torque control (DTC), and model predictive control (MPC).

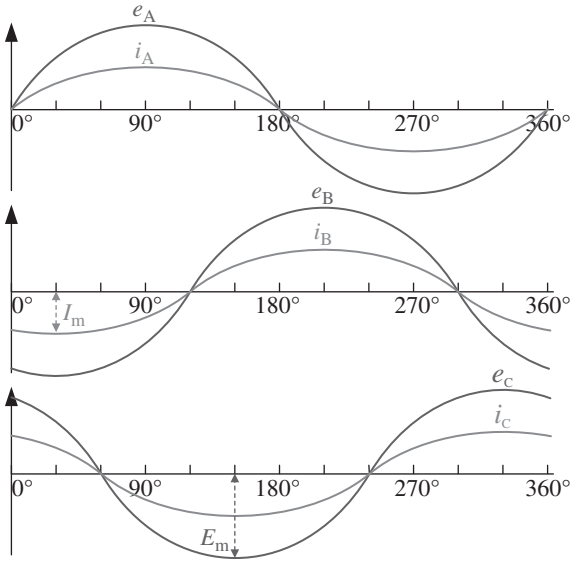

Figure 1.10 Sinusoidal back-EMF waveforms and sine-wave phase currents of BLAC drive.

1.3.2.1 Space Vector PWM

For BLAC drives, SVPWM is a popular technique used to control the output voltage of the VSI to drive the machine at the desired speed and torque [11]–[13].

As shown in Figure 1.6, S_A, S_B, S_C are the switching states of the three legs of the VSI. To avoid the short circuit, the upper and lower switches in one leg work in the complementary mode with a deadtime. Therefore, if the upper switch is on and the lower switch is off, the value of the switching state is "1", and if the upper switch is off and the lower switcher is on, the value of the switching state is "0". In total, there are eight switching states of the VSI as depicted in Figure 1.11. For all

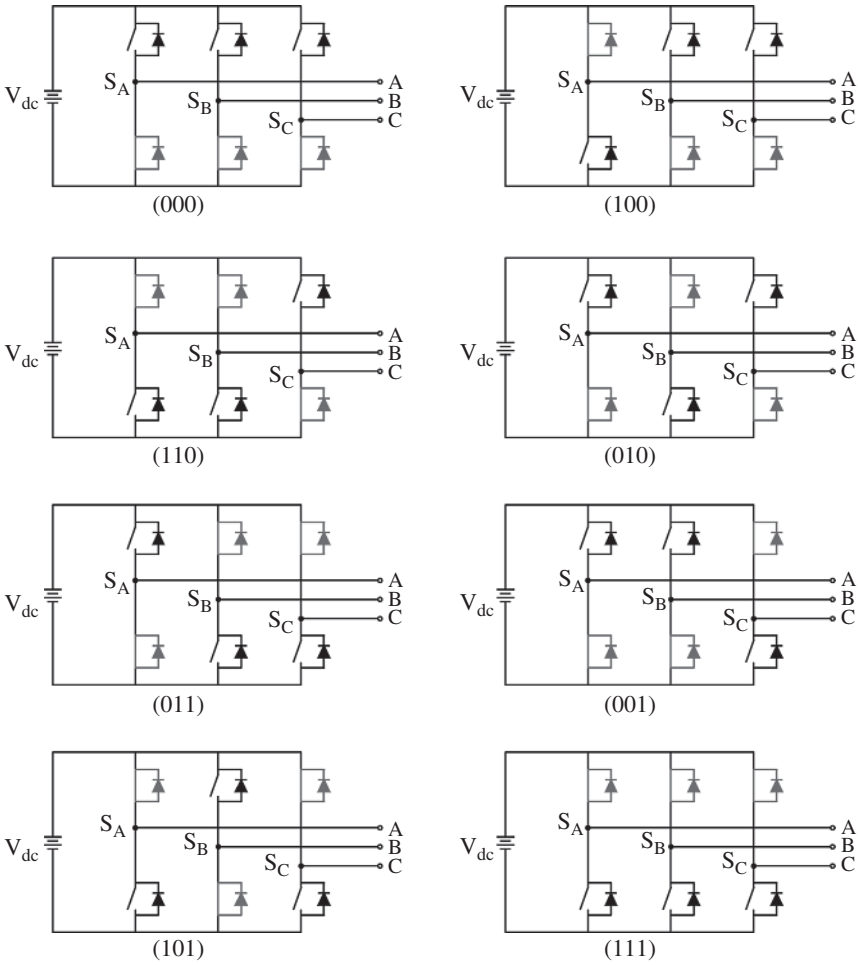

Figure 1.11 Block diagram of VSI at different switching states.

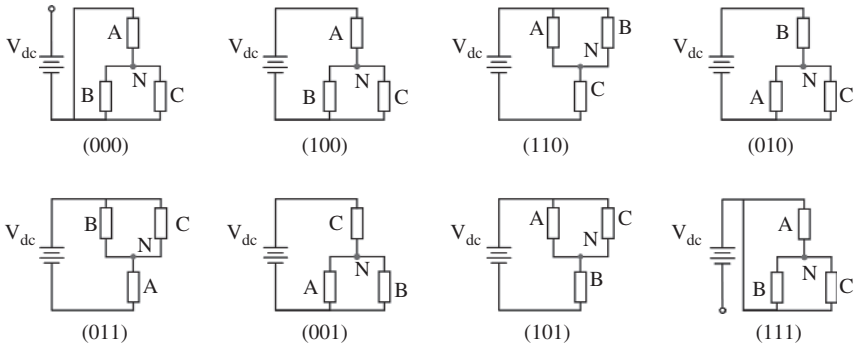

Figure 1.12 Equivalent circuits of switching states.

switching states, the corresponding equivalent circuits including the PM machine are shown in Figure 1.12. Based on the equivalent circuits, the three-phase voltages for all switching states can be derived as shown in Table 1.1.

SVPWM is based on the concept of a rotating space vector [14]. For VSI, the three-phase voltages can form an equivalent voltage vector v_s as:

$$\mathbf{v}_s = v_{\mathrm{AN}} + v_{\mathrm{BN}} e^{j\frac{2}{3}\pi} + v_{\mathrm{CN}} e^{j\frac{4}{3}\pi} \tag{1.16}$$

where v_{AN}, v_{BN}, v_{CN} are the phase voltages of a PM machine in the ABC reference frame. The voltage vector in (1.16) can also be represented in the stationary reference frame as:

$$\mathbf{v}_s = v_{\mathrm{AN}} + v_{\mathrm{BN}} e^{j\frac{2}{3}\pi} + v_{\mathrm{CN}} e^{j\frac{4}{3}\pi} = v_\alpha + j v_\beta \tag{1.17}$$

Table 1.1 Switching states and corresponding phase voltages of VSI.

Switching state (S_A S_B S_C)	**000**	**100**	**110**	**010**	**011**	**001**	**101**	**111**
v_{AN}	0	$\frac{2}{3}V_{\mathrm{dc}}$	$\frac{1}{3}V_{\mathrm{dc}}$	$-\frac{1}{3}V_{\mathrm{dc}}$	$-\frac{2}{3}V_{\mathrm{dc}}$	$-\frac{1}{3}V_{\mathrm{dc}}$	$\frac{1}{3}V_{\mathrm{dc}}$	0
v_{BN}	0	$-\frac{1}{3}V_{\mathrm{dc}}$	$\frac{1}{3}V_{\mathrm{dc}}$	$\frac{2}{3}V_{\mathrm{dc}}$	$\frac{1}{3}V_{\mathrm{dc}}$	$-\frac{1}{3}V_{\mathrm{dc}}$	$-\frac{2}{3}V_{\mathrm{dc}}$	0
v_{CN}	0	$-\frac{1}{3}V_{\mathrm{dc}}$	$-\frac{2}{3}V_{\mathrm{dc}}$	$-\frac{1}{3}V_{\mathrm{dc}}$	$\frac{1}{3}V_{\mathrm{dc}}$	$\frac{2}{3}V_{\mathrm{dc}}$	$\frac{1}{3}V_{\mathrm{dc}}$	0

Table 1.2 Switching states and voltage vectors of VSI.

Switching state (S_A S_B S_C)	000	100	110	010	011	001	101	111
Voltage vector	$\mathbf{v}_0$	$\mathbf{v}_1$	$\mathbf{v}_2$	$\mathbf{v}_3$	$\mathbf{v}_4$	$\mathbf{v}_5$	$\mathbf{v}_6$	$\mathbf{v}_7$
Value	0	$\frac{2}{3}V_{\mathrm{dc}}e^{j0}$	$\frac{2}{3}V_{\mathrm{dc}}e^{j\frac{1}{3}\pi}$	$\frac{2}{3}V_{\mathrm{dc}}e^{j\frac{2}{3}\pi}$	$\frac{2}{3}V_{\mathrm{dc}}e^{j\pi}$	$\frac{2}{3}V_{\mathrm{dc}}e^{j\frac{4}{3}\pi}$	$\frac{2}{3}V_{\mathrm{dc}}e^{j\frac{5}{3}\pi}$	0

Considering the eight switching states of the VSI, there are eight basic voltage vectors in total including six active vectors, i.e. $\mathbf{v}_{1,\ldots6}$, and two zero vectors, i.e. $\mathbf{v}_{0,7}$. The eight basic voltage vectors for different switching states are summarized in Table 1.2.

As shown in Figure 1.13, in the stationary reference frame, the active voltage vectors form a hexagon with an amplitude of $2V_{dc}/3$, and the whole area is divided into six sectors by the voltage vectors.

Based on the eight basic voltage vectors $\mathbf{v}_{0,\ldots7}$, the VSI can generate any rotating voltage vector by synthesizing two adjacent active vectors and a zero vector within a sampling period T_s. For example, as shown in Figure 1.13, a reference voltage vector $\mathbf{v}_s^*$ in Sector I is given, with two active vectors $\mathbf{v}_1$, $\mathbf{v}_2$ and the zero vector $\mathbf{v}_0$ are used for the synthesis. The synthesis is based on the volt-second balancing, which can be expressed as:

$$\mathbf{v}_s^* T_s = \mathbf{v}_1 T_1 + \mathbf{v}_2 T_2 + \mathbf{v}_0 T_0 \tag{1.18}$$

$$T_s = T_1 + T_2 + T_0 \tag{1.19}$$

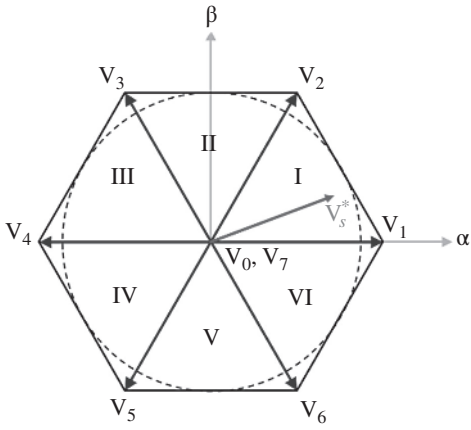

Figure 1.13 Voltage vectors.

where T_1, T_2, and T_0 are the durations of the voltage vectors $\mathbf{v}_1$, $\mathbf{v}_2$, and $\mathbf{v}_0$, respectively. Furthermore, the synthesis is illustrated in Figure 1.14.

Accordingly, the duration time for each vector can be derived as:

$$\begin{cases} T_1 = \dfrac{\sqrt{3}V_s^*}{V_{dc}} T_s \sin\left(\dfrac{\pi}{3} - \theta\right) \\ T_2 = \dfrac{\sqrt{3}V_s^*}{V_{dc}} T_s \sin(\theta), \quad 0 \le \theta \le \dfrac{\pi}{3} \\ T_0 = T_s - T_1 - T_2 \end{cases} \tag{1.20}$$

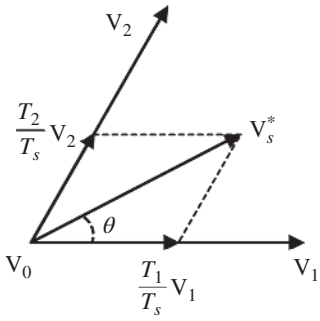

Figure 1.14 Stator voltage reference vector in Sector I.

where V_s^* is the magnitude of the stator voltage reference, and θ is the angle of the stator voltage reference. For the cases in other sectors, the duration time can be derived similarly.

After obtaining the durations of voltage vectors, the next step is to determine the switching sequence. The optimum switching sequence of SVPWM [11] is commonly used. An example of the switching sequence in Sector I is depicted in Figure 1.15. To reduce the switching losses, the transition from one switching state to the next is performed by switching only one leg. Therefore, the zero vector $\mathbf{v}_7$ is applied in the middle instead of the zero vector $\mathbf{v}_0$. Moreover, as shown in Figure 1.15, zero vectors are allocated to produce a symmetrical PWM so that the harmonic distortion in the output voltage can be minimized.

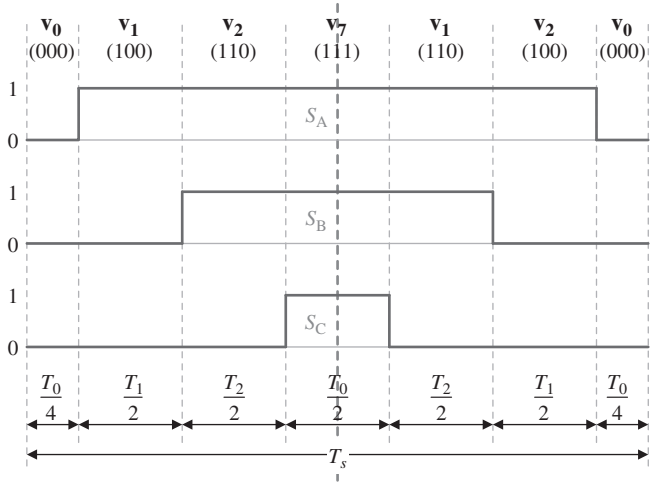

Figure 1.15 Switching pattern for SVPWM in Sector I.

When the reference voltage vector is within the inscribed circle of the hexagon, the trajectory of the rotating voltage vector generated by the SVPWM algorithm can be a circle within the hexagon, as in Figure 1.13. This ensures that the fundamental components of the output three-phase voltages are sine waves with a constant amplitude and frequency. However, if the reference voltage vector is outside the inscribed circle of the hexagon, over-modulation schemes [11], [13] need to be used to generate the desired output voltage.

1.3.2.2 Field-Oriented Control

FOC, or vector control (VC), was initially developed in the early 1970s [15], [16]. By adopting FOC, the three-phase alternative current (AC) machine can be controlled as a separately excited direct current (dc) machine. As described in Section 1.3.1.3, based on the reference frame transformation, the three-phase sinusoidal stator currents are transformed into two orthogonal dc components: one defines the magnetic flux and the other defines the torque. With FOC, an excellent performance of the PMSM (BLAC) drive is achieved. The PMSMs can operate over the full speed range and provide desired torque control performance even at zero speed. In addition, FOC shows good dynamic performance and control accuracy.

The block diagram of a typical FOC used for PMSM speed control is shown in Figure 1.16. The *q*-axis current is related to the torque and the *d*-axis current is related to the flux, and they can be regulated separately [17]. As shown in Figure 1.16, a SVPWM module is employed in the PMSM drives. As introduced in Section 1.3.2.1, the stator voltage reference generated by the current controller can be applied to the machine by SVPWM.

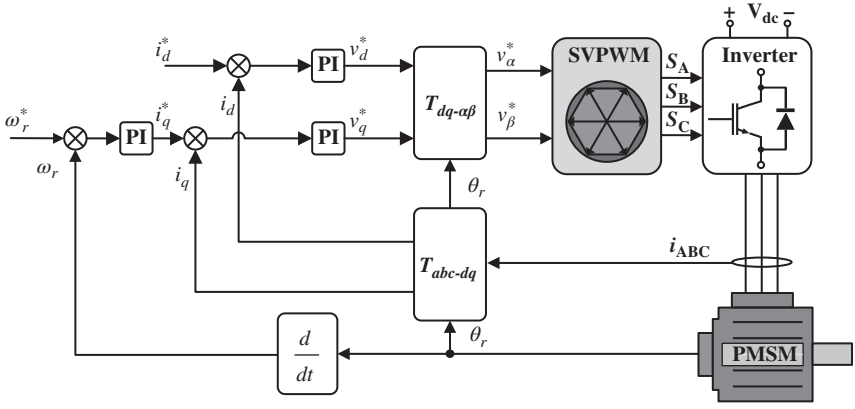

Figure 1.16 Block diagram of field-oriented control.

1.3.2.3 Direct Torque Control

DTC has been developed due to its simple structure, excellent transient response, and good robustness against rotor parameters. DTC was first proposed in [18]–[21] for induction machines and has been extended to other machines, such as PMSMs [22]. Based on the stator currents and voltages, the flux and electromagnetic torque are estimated at first. Then, hysteresis regulators are usually implemented in the conventional switching table-based DTC strategy for the regulation of both electromagnetic torque and stator flux as shown in Figure 1.17. The switching table for DTC is given in Table 1.3, in which ε_T and ε_ψ are the torque and flux error output by hysteresis controllers. The voltage vectors for each case of ε_T and ε_ψ at different rotor positions are listed together with corresponding switching states of the inverter in the parentheses.

Compared to the FOC, coordinate transformations and specific modulations are not required. Hence, the transient torque control performance can be significantly improved. However, in a digital controller, the responses of both torque and stator flux controllers can exceed the predefined hysteresis bands due to the time delay and the fixed sampling frequency, potentially leading to large torque and stator flux ripples. In order to reduce the torque and flux ripples, DTC with SVPWM [23]–[25] can be used with a fixed switching frequency.

1.3.2.4 Model Predictive Control

The advancements in fast and powerful microprocessors have led to increased interest in utilizing MPC for PMSM drive systems [26]–[29]. Research on PMSM drives has focused primarily on predictive current control, predictive torque

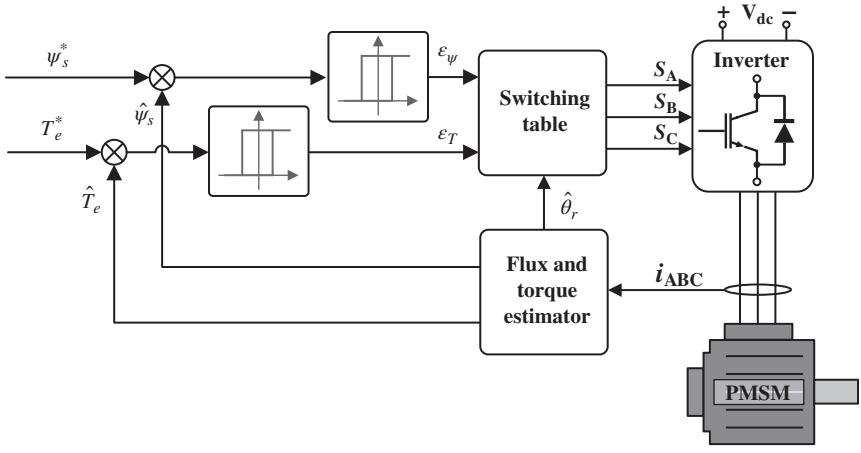

Figure 1.17 Block diagram of direct torque control.

Table 1.3 Switching table of DTC.

		Rotor position					
ε_ψ	ε_T	330–30°	30–90°	90–150°	150–210°	210–270°	270–330°
1	1	$\mathbf{v}_2(110)$	$\mathbf{v}_3(010)$	$\mathbf{v}_4(011)$	$\mathbf{v}_5(001)$	$\mathbf{v}_6(101)$	$\mathbf{v}_1(100)$
	0	$\mathbf{v}_6(101)$	$\mathbf{v}_1(100)$	$\mathbf{v}_2(110)$	$\mathbf{v}_3(010)$	$\mathbf{v}_4(011)$	$\mathbf{v}_5(001)$
0	1	$\mathbf{v}_3(010)$	$\mathbf{v}_4(011)$	$\mathbf{v}_5(001)$	$\mathbf{v}_6(101)$	$\mathbf{v}_1(100)$	$\mathbf{v}_2(110)$
	0	$\mathbf{v}_5(001)$	$\mathbf{v}_6(101)$	$\mathbf{v}_1(100)$	$\mathbf{v}_2(110)$	$\mathbf{v}_3(010)$	$\mathbf{v}_4(011)$

control, and predictive speed control [29]. A typical model of predictive current control of PMSM is shown in Figure 1.18.

Based on the machine model and the current at the kth sampling instant, i.e. $i_{dq}(k)$, the current at the $(k+1)$th sampling instant, i.e. $i_{dq}(k+1)$, is predicted iteratively with different inverter switching states. Based on the machine model in Section 1.3.1.3, the prediction model can be expressed as:

$$\begin{bmatrix} i_d^p(k+1) \\ i_q^p(k+1) \end{bmatrix} = \begin{bmatrix} 1-\dfrac{T_s}{L_s}R_s & \omega_r T_s \\ -\omega_r T_s & 1-\dfrac{T_s}{L_s}R_s \end{bmatrix} \begin{bmatrix} i_d(k) \\ i_q(k) \end{bmatrix} + \begin{bmatrix} \dfrac{T_s}{L_s} & 0 \\ 0 & \dfrac{T_s}{L_s} \end{bmatrix} \begin{bmatrix} v_d(k) \\ v_q(k) \end{bmatrix} + \begin{bmatrix} 0 \\ -\dfrac{T_s}{L_s}\omega_r \psi_m \end{bmatrix} \tag{1.21}$$

where T_s is the sampling period.

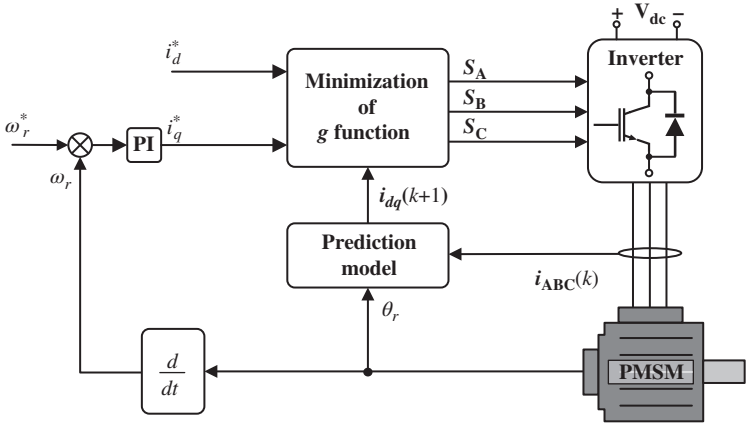

Figure 1.18 Block diagram of model predictive current control.

Then, a cost function in (1.22) is designed to select the voltage vector that minimizes the error between the reference current and the predicted current.

$$g = \left|i_d^* - i_d^p(k+1)\right| + \left|i_q^* - i_q^p(k+1)\right| \tag{1.22}$$

The dynamics of the MPC are desirable as it utilizes predictive variables to determine the switching state, avoiding the need for PWM. However, a major issue of MPC is the current tracking error caused by uncertainties in the model. To address this issue, additional compensations are required.

1.4 Basic Principle of PM BLDC Drives

1.4.1 Modeling

As with the BLAC drives, to simplify the modeling, the same assumptions of BLAC drives in Section 1.3 are made for BLDC drives. Then, the BLDC three-phase stator voltage equations can be expressed as:

$$\begin{bmatrix} v_{\mathrm{A}} \\ v_{\mathrm{B}} \\ v_{\mathrm{C}} \end{bmatrix} = \begin{bmatrix} R_s & 0 & 0 \\ 0 & R_s & 0 \\ 0 & 0 & R_s \end{bmatrix} \cdot \begin{bmatrix} i_{\mathrm{A}} \\ i_{\mathrm{B}} \\ i_{\mathrm{C}} \end{bmatrix} + p \begin{bmatrix} L_{\mathrm{AA}} & M_{\mathrm{AB}} & M_{\mathrm{AC}} \\ M_{\mathrm{BA}} & L_{\mathrm{BB}} & M_{\mathrm{BC}} \\ M_{\mathrm{CA}} & M_{\mathrm{CB}} & L_{\mathrm{CC}} \end{bmatrix} \cdot \begin{bmatrix} i_{\mathrm{A}} \\ i_{\mathrm{B}} \\ i_{\mathrm{C}} \end{bmatrix} + \begin{bmatrix} e_{\mathrm{A}} \\ e_{\mathrm{B}} \\ e_{\mathrm{C}} \end{bmatrix} \tag{1.23}$$

where e_{A}, e_{B}, e_{C} are the three-phase back-EMFs.

For BLDC machines in which PMs are often surface-mounted, it can be assumed that there is no change in the inductance with rotor position and the three phases are symmetrical. Then, the self- and mutual-inductances can be represented as:

$$L_{\mathrm{AA}} = L_{\mathrm{BB}} = L_{\mathrm{CC}} = L, \;\; M_{\mathrm{AB}} = M_{\mathrm{BA}} = M_{\mathrm{BC}} = M_{\mathrm{CB}} = M_{\mathrm{AC}} = M_{\mathrm{CA}} = M \tag{1.24}$$

Therefore, (1.23) can be re-written as:

$$\begin{bmatrix} v_{\mathrm{A}} \\ v_{\mathrm{B}} \\ v_{\mathrm{C}} \end{bmatrix} = \begin{bmatrix} R_s & 0 & 0 \\ 0 & R_s & 0 \\ 0 & 0 & R_s \end{bmatrix} \cdot \begin{bmatrix} i_{\mathrm{A}} \\ i_{\mathrm{B}} \\ i_{\mathrm{C}} \end{bmatrix} + \begin{bmatrix} L & M & M \\ M & L & M \\ M & M & L \end{bmatrix} \cdot p \begin{bmatrix} i_{\mathrm{A}} \\ i_{\mathrm{B}} \\ i_{\mathrm{C}} \end{bmatrix} + \begin{bmatrix} e_{\mathrm{A}} \\ e_{\mathrm{B}} \\ e_{\mathrm{C}} \end{bmatrix} \tag{1.25}$$

Since the three phase currents are balanced, i.e. $i_A + i_B + i_C = 0$, (1.25) can be further simplified as:

$$\begin{bmatrix} v_A \\ v_B \\ v_C \end{bmatrix} = \begin{bmatrix} R_s & 0 & 0 \\ 0 & R_s & 0 \\ 0 & 0 & R_s \end{bmatrix} \cdot \begin{bmatrix} i_A \\ i_B \\ i_C \end{bmatrix} + \begin{bmatrix} L-M & 0 & 0 \\ 0 & L-M & 0 \\ 0 & 0 & L-M \end{bmatrix} \cdot p \begin{bmatrix} i_A \\ i_B \\ i_C \end{bmatrix} + \begin{bmatrix} e_A \\ e_B \\ e_C \end{bmatrix} \tag{1.26}$$

Ideally, the three-phase back-EMFs are trapezoidal as shown in Figure 1.7.

1.4.2 Control Strategies

In the BLDC operation, the three-phase current should be aligned with the back-EMF so that the angle between the stator flux and the rotor flux is kept within the range from 60° to 120° to produce the maximum torque. Generally, two-phase 120° conduction six-step control is employed in BLDC operation, which is shown in Figure 1.19. As can be seen, the phase current is switched on 30° after the zero-crossing of its phase back-EMF waveform.

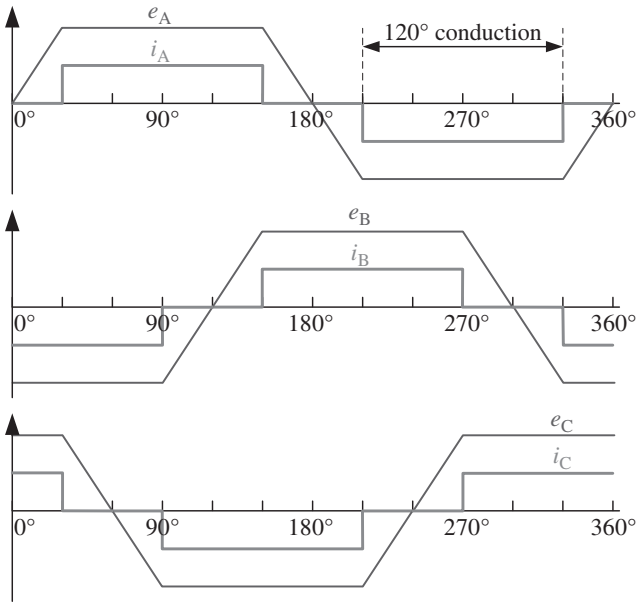

Figure 1.19 Illustration of 120° conduction six-step control strategies.

In the two-phase 120° conduction six-step control, a fundamental cycle is divided into six sectors as shown in Figure 1.2a. In each sector, two of the three phases are conducted and the third phase is floating. For each phase, it is switched on for 120° and is then switched off for 60°. In this 60° floating interval, the back-EMF can be measured, which provides a way to detect the rotor position.

Figure 1.20 shows a block diagram for the 120° conduction six-step control, where ω_r is the machine speed and i_{dc} is the dc-link current. The superscript * denotes the reference value.

As shown in Table 1.4, six sectors are defined according to the rotor position, which determines the conduction modes of the three phases. The conduction sequence across the six sectors is stored in the commutation logic block in Figure 1.20.

The standard control system of 120° conduction six-step control contains two control loops, i.e. the outer loop for speed control and the inner loop for current control, which are connected in cascade. The measured and estimated mechanical and electrical variables are fed back in each closed loop. The output of the speed

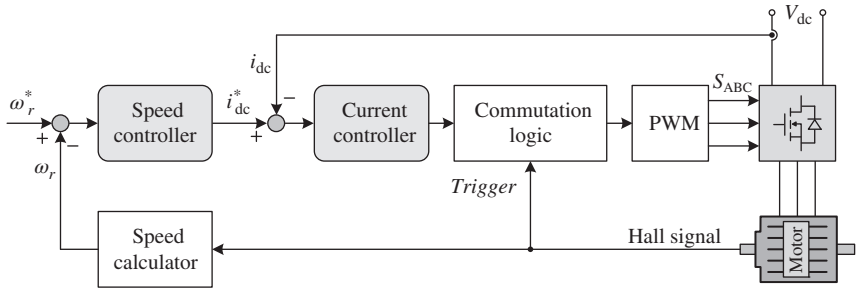

Figure 1.20 Block diagram of BLDC operation based on six-step control.

Table 1.4 Definition of sectors and conduction modes.

Sector	Rotor position (°)	Positive phase	Negative phase	Floating phase
I	30–90	A	B	C
II	90–150	A	C	B
III	150–210	B	C	A
IV	210–270	B	A	C
V	270–330	C	A	B
VI	330–30	C	B	A

controller is the reference input of the current controller i_{dc}^*. By adjusting the PWM duty ratio (output voltage), the feedback current i_{dc} can track the reference input i_{dc}^* and the feedback speed ω_r can track the reference input ω_r^*. That is the mechanism of the typical 120° conduction six-step control. Since the time constant of electrical variables (resistance and inductance) is far lower than the one of mechanical variables, the inner loop is much faster than the outer loop. In this way, there are no interferences between the current and speed controllers, and thus, they can be designed and tuned independently.

For the current control loop, since only two phases are conducted, the stator current can be directly reflected on the dc-link. For low-cost applications, the dc-link current signal is usually utilized in the current control loop. For the speed control loop, the machine speed and rotor position (commutation instants) information can be derived from position sensors. As shown in Figure 1.20, for a sensored BLDC drive, the commutation is often triggered by the Hall-effect sensors. The machine speed can be calculated from the time duration between two subsequent transitions of Hall-effect sensors. For sensorless operation of BLDC drives, refer to Chapters 10 and 11.

1.5 Comparison Between PM BLDC (PMSM) and BLAC Drives

A brief comparison between BLDC and BLAC operation modes is given in Table 1.5.

In practice, the back-EMF may be significantly different from the ideal waveforms. Besides, the selection of BLDC or BLAC operation mode also depends on the specific application. Various factors should be taken into consideration, e.g. the implementation complexity, the system cost, the performance demand, etc. Hence, irrespective of the back-EMF waveforms, the PM brushless machines may be operated in either BLDC or BLAC mode.

1.5.1 Square-Wave Back-EMF Machine

Ideally, a square-wave back-EMF machine should be operated in the BLDC mode. By way of example, if both the phase current and back-EMF are of ideal waveforms, as shown in Figure 1.7a, i.e. the back-EMF is trapezoidal with a flat top of 120° electrically, while the current waveform is square-wave, the electromagnetic torque of a BLDC machine will be free of ripple, and can be expressed as:

$$T_{m\_BLDC} = \frac{2E_m I_m}{\omega_m} \tag{1.27}$$

Table 1.5 Comparison between BLDC and BLAC operation [30].

	BLDC operation	BLAC operation
Control variable	Square-wave current	Sine-wave current
Position sensor resolution	Low	High
Ripple in electromagnetic torque	High or moderate[a]	Low
Speed and/or position control	Coarse	Precise
Inverter switching loss[b]	Low	High
Current harmonics	High	Low
Control simplicity	Simple	Complicated
Flux-weakening capability [31][c]	Low	High

[a] Because the ideal square-wave back-EMF waveform is difficult to achieve in practical machines.
[b] In BLDC operation, there is switching loss in one or two power electronic devices, depending on how PWM is applied. In BLAC operation there is switching loss in all six devices at any instant.
[c] Assuming the same machine running in BLDC and BLAC modes, respectively.

where ω_m is the mechanical angular speed. Both the phase current and back-EMF are rich in harmonics, as listed in Table 1.6. The interaction between current and back-EMF harmonics of the same order will result in an effective magnetic torque, as also listed in Table 1.6.

From Table 1.6, it can be seen that:

- There is no third harmonic in the phase current, but the higher order harmonics are significant.
- The most significant harmonic in the phase back-EMF is the third harmonic, while the higher harmonics are relatively low. However, the third-harmonic

Table 1.6 Harmonics of back-EMF and phase current, and electromagnetic torque due to the same-order harmonics in an ideal BLDC drive [30].

Order of harmonic (ν)	Amplitude of back-EMF harmonics ($E_{m\nu}/E_m$) (%)	Amplitude of phase current harmonics ($I_{m\nu}/I_m$) (%)	Torque due to same-order harmonics ($T_{m\nu}/T_m$) (%)
1	121.6	110.3	100.6
3	27.0	0	0
5	4.9	−22.1	−0.8
7	−2.5	−15.8	0.3
...	...	...	...

Table 1.7 Current and torque comparison for a square-wave back-EMF machine in BLDC and BLAC modes [30].

Amplitude of 120°-trapezoidal back-EMF			E_m	
BLDC operation	Amplitude of square-wave phase current		I_m	
	Electromagnetic torque		$2\,E_m\,I_m/\Omega$	
BLAC operation	Amplitude of sine-wave phase current	$1.096\,I_m$	I_m	$1.155\,I_m$
	Electromagnetic torque	$2\,E_m\,I_m/\omega_m$	$1.825\,E_m\,I_m/\omega_m$	$2.107\,E_m\,I_m/\omega_m$
	Condition	Same torque as BLDC operation	Same current peak as BLDC operation	Same current RMS as BLDC operation

back-EMF does not contribute to the electromagnetic torque. Therefore, only the fundamental component of the back-EMF is dominant.

- The effective electromagnetic torque is produced mainly by the interaction between the fundamental back-EMF and current. High-order harmonics produce little effective electromagnetic torque.

In practical applications, the square-wave machine can also operate in the BLAC mode. A performance comparison is listed in Table 1.7.

1.5.2 Sine-Wave Back-EMF Machine

A sine-wave machine should ideally operate in the BLAC mode. When both the phase current and back-EMF are ideal sinusoidal waveforms, as shown in Figure 1.7b, the electromagnetic torque will be ripple free, and can be expressed as:

$$T_{m\_\mathrm{BLAC}} = \frac{3E_m I_m}{2\omega_m} \tag{1.28}$$

However, in practical applications it can also be operated in the BLDC mode, since there is no third harmonic in the phase current while the higher harmonics are usually low. Hence, the fundamental component of current is dominant. In such a case, the performance comparison is listed in Table 1.8.

Table 1.8 Current and torque comparison for a sine-wave back-EMF machine in BLAC and BLDC modes [30].

Amplitude of sinusoidal back-EMF		E_m		
BLAC operation	Amplitude of sine-wave phase current	I_m		
	Electromagnetic torque	$1.5\,E_m\,I_m\,/\omega_m$		
BLDC operation	Amplitude of square-wave phase current	$0.907\,I_m$	I_m	$0.866\,I_m$
	Electromagnetic torque	$1.5\,E_m\,I_m\,/\omega_m$	$1.654\,E_m\,I_m\,/\omega_m$	$1.432\,E_m\,I_m\,/\omega_m$
	Condition	Same torque as BLAC operation	Same current peak as BLAC operation	Same current RMS as BLAC operation

Note that if a square-wave machine is operated in the BLAC mode, or a sine-wave machine is run in the BLDC mode, or if the machine back-EMF waveform is neither a pure sine wave nor a pure square wave or trapezoidal waveform with 120^o flat top, torque ripples will arise. In some machines, the line-to-neutral back-EMF waveform is not sinusoidal since it contains zero sequence harmonics, such as the third harmonic. However, the line-to-line back-EMF waveform can be sinusoidal, since zero sequence harmonics do not exist. Such machines are still eminently suitable for BLAC operation.

1.6 Sensorless Control Techniques and Applications

High-performance PM machine drives need rotor position information. They are usually obtained by employing a hardware rotor position sensor, such as a resolver, encoder, Hall effect sensor, etc. However, doing so will increase the size and reduce the reliability particularly under harsh environments. It is always desirable to eliminate the rotor hardware rotor position sensor by using software-based sensorless techniques [32].

1.6.1 Classification

There are various sensorless control methods, and a brief classification of sensorless control techniques for BLAC and BLDC drives is shown in Figure 1.21.

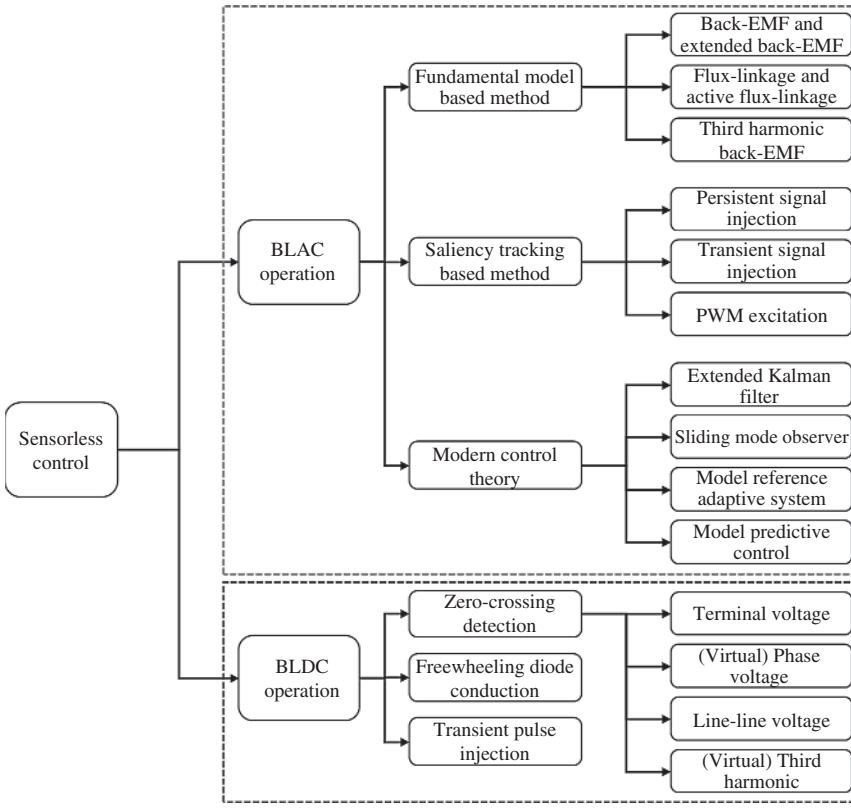

Figure 1.21 Classification of sensorless control techniques for PM machines.

For BLAC operation, fundamental model-based methods are based on the back-EMF or flux-linkage; accurate parameters and observable machine model are necessary. Therefore, they are preferred in middle and high-speed ranges. For SPMs, back-EMF and flux-linkage can be utilized, while for IPMs, the extended back-EMF and active flux-linkage are used for sensorless control. Apart from the fundamental component, the third harmonic of back-EMF and flux-linkage can also be used for position estimation. For saliency-based methods, the PM machine saliency is independent of the rotor speed. With different signal injection methods, this type of method can be used in zero and low-speed ranges. Moreover, modern control theories such as the extended Kalman filter (EKF), sliding mode observer (SMO), and model adaptive reference system (MRAS) can be applied to conventional sensorless techniques to enhance the estimation performance.

For BLDC operation, the zero-crossing points (ZCPs) detection-based method is widely adopted, which provides a good performance at middle and high speeds since it relies on the amplitude of the back-EMF. The back-EMF can be measured in various ways as shown in Figure 1.21. Moreover, the freewheeling diode conduction is another way to indirectly detect the ZCPs. To detect the rotor position at zero speed, the transient pulse injection-based method can be employed.

1.6.2 Applications

In general, sensorless techniques have proven to be highly effective for applications with low torque requirements at start-up. In recent years, these techniques have been successfully commercialized for a variety of applications, including ventilation fans, pumps, vacuum cleaners, hand dryers, hair dryers, and, more recently, wind power generators. Despite this success, the use of sensorless control for applications that require high torque for regular starting, such as general industrial drives and electric vehicle propulsion, remains challenging.

However, there have been successful developments in the use of sensorless control for commercial washing machines by utilizing high-frequency signal injection for starting since the starting period is not so critical, although it is desirable that it be as short as possible. Researchers are continuing to investigate the potential of this technology for electric vehicles, with extensive research activities currently underway. It is anticipated that over the next five to ten years, sensorless control will be increasingly used for fault-tolerance drives in electric vehicles and aerospace applications, as researchers work to improve the technology and address the challenges associated with high-torque applications.

Despite the current limitations of sensorless control techniques, they offer numerous advantages over traditional methods that rely on sensors. For example, sensorless control can reduce costs and complexity by eliminating the need for dedicated sensors, while also improving reliability by reducing the number of failure points in the system. As the technology continues to evolve and improve, it is likely that sensorless control will find even broader application, offering a reliable, cost-effective, and efficient solution for a wide range of industrial and commercial needs.

1.7 Scope of This Book

In this book, the basic principles and the state-of-the-art position sensorless control techniques for PM machine drives will be described, including both PM BLAC and BLDC drives, single three-phase PM machines, dual three-phase PM

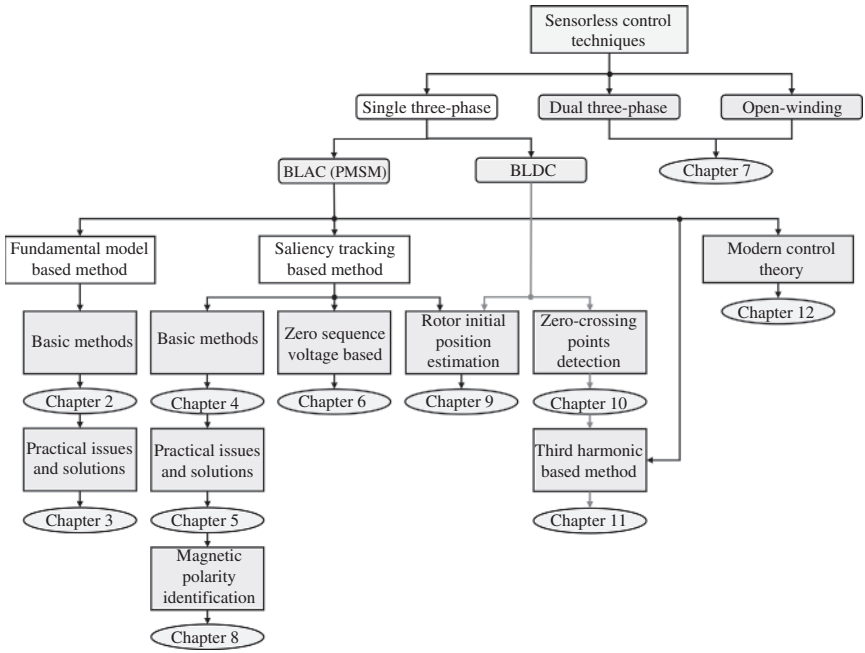

Figure 1.22 Scope of this book.

machines, and open-winding PM machines. The overall scope of this book is illustrated in Figure 1.22.

For PM BLAC drives, Chapter 2 covers the fundamental model-based methods, including flux observer, active flux observer, back-EMF, and extended back-EMF. Chapter 3 presents practical issues and corresponding solutions, e.g. integration drifting and filter phase delay, back-EMF and current harmonics, cross-coupling magnetic saturation, parameter mismatch, asymmetric parameters, etc. For the saliency tracking-based method, Chapter 4 introduces the basic methods using high-frequency signal injection in various reference frames according to injection signal and response voltage and current types, such as rotating, pulsating, and square wave. In Chapter 5, special issues of the saliency tracking-based method will be fully discussed, including various parasitic effect issues and solutions, e.g. cross-coupling magnetic saturation, multi-saliency, asymmetric parameters, inverter nonlinearity, signal delay, machine design, load effect, etc. For high-frequency signal injection, the methods for selecting the amplitudes and frequencies for injection signals will be systematically described. Moreover, for the saliency tracking-based method, the utilization of the zero-sequence voltage is

described in Chapter 6. Apart from single three-phase PM machines, sensorless techniques for dual three-phase machines and open-winding machines are detailed in Chapter 7. Further, comprehensive techniques for detecting rotor magnetic polarity and initial rotor position will be introduced in Chapters 8 and 9, respectively.

For PM BLDC drives, sensorless techniques for detecting zero crossing of back-EMF waveforms under voltage and current PWM control will be described in Chapter 10, together with those based on third harmonic back-EMF in Chapter 11, which is also applicable to BLAC drives.

Finally, in Chapter 12, this book will also highlight some modern control theory-based sensorless techniques, including model reference adaptive system, sliding mode, EKF, and MPC.

References

1 Z. Q. Zhu and D. Howe, "Electrical machines and drives for electric, hybrid, and fuel cell vehicles," *Proc. IEEE*, vol. 95, no. 4, pp. 746–765, Apr. 2007.

2 J. R. Hendershot and T. J. E. Miller, *Design of Brushless Permanent-magnet Motors*. Oxford, UK: Magna Physics and Oxford Science Publications, 1994.

3 J. F. Gieras, R. Wang, and M. J. Kamper, *Axial Flux Permanent Magnet Brushless Machines*. Dordrecht, Netherlands: Springer, 2008.

4 H. Weh and H. May, "Achievable force densities for permanent magnet excited machines in new configurations," *Proc. Int. Conf. Elect. Mach. Drives*, pp. 1107–1111, 1986.

5 H. Weh and J. Jiang, "Calculation and design consideration for synchronous machines with transverse flux configuration," *Archiv fur Elektrotechnik*, vol. 71, pp. 187–198, 1988.

6 D. Ishak, Z. Q. Zhu, and D. Howe, "Comparison of PM brushless motors, having either all teeth or alternate teeth wound," *IEEE Trans. Energy Convers.*, vol. 21, no. 1, pp. 95–106, Mar. 2006.

7 A. M. EL-Refaie, "Fractional-slot concentrated-windings synchronous permanent magnet machines: opportunities and challenges," *IEEE Trans. Ind. Electron.*, vol. 57, no. 1, pp. 107–121, Jan. 2010.

8 G. Dajaku, W. Xie, and D. Gerling, "Reduction of low space harmonics for the fractional slot concentrated windings using a novel stator design," *IEEE Trans. Magn.*, vol. 50, no. 5, pp. 1–12, May 2014.

9 P. Pillay and R. Krishnan, "Modeling, simulation, and analysis of permanent-magnet motor drives. I. The permanent-magnet synchronous motor drive," *IEEE Trans. Ind. Appl.*, vol. 25, no. 2, pp. 265–273, Mar. 1989.

10 P. Pillay and R. Krishnan, "Modeling, simulation, and analysis of permanent-magnet motor drives. II. The brushless dc motor drive," *IEEE Trans. Ind. Appl.*, vol. 25, no. 2, pp. 274–279, Mar. 1989.

11 H. W. van der Broeck, H.-C. Skudelny, and G. V. Stanke, "Analysis and realization of a pulse width modulator based on voltage space vectors," *IEEE Trans. Ind. Appl.*, vol. 24, no. 1, pp. 142–150, Jan. 1988.

12 O. Ogasawara, H. Akagi, and A. Nabae, "A novel PWM scheme of voltage source inverters based on space vector theory," *EPE Eur. Conf. Power Electron. Appl.*, Aachen, Germany, 1989, pp. 1197–1202.

13 J. Holtz, "Pulsewidth modulation–-a survey," *IEEE Trans. Ind. Elect.*, vol. 39, no. 5, pp. 410–420, Oct. 1992, https://doi.org/10.1109/41.161472.

14 K. P. Kovacs and I. Racz, *Transiente Vorgange in Wechselstrom-maschinen*, vol. I and II. Budapest, Hungary: Verlag d. Ungar. Akad. d. Wissensch, 1959.

15 F. Blaschke, "The principle of field orientation as applied to the new transvector closed loop control system for rotating field machines," *Siemens Rev.*, vol. 34, pp. 217–220, 1972.

16 K. H. Bayer, H. Waldmann, and M. Weibelzahl, "Field-oriented closed-loop control of a synchronous machine with the new transvector control system," *Siemens Rev.*, vol. 39, pp. 220–223, 1972.

17 P. Vas, *Sensorless Vector and Direct Torque Control*. Oxford, UK: Oxford Univ. Press, 2003.

18 I. Takahashi and T. Noguchi, "A new quick-response and high efficiency control strategy of an induction-motor," *IEEE Trans. Ind. Appl.*, vol. 22, no. 5, pp. 820–827, 1986.

19 I. Takahashi and Y. Ohmori, "High-performance direct torque control of an induction motor," *IEEE Trans. Ind. Appl.*, vol. 25, no. 2, pp. 257–264, Mar. 1989.

20 M. Depenbrock, "Direct self-control (DSC) of inverter-fed induction machine," *IEEE Trans. Power Electron.*, vol. 3, no. 4, pp. 420–429, 1988.

21 U. Baader, M. Depenbrock, and G. Gierse, "Direct self control (DSC) of inverter-fed induction machine: a basis for speed control without speed measurement," *IEEE Trans. Ind. Appl.*, vol. 28, no. 3, pp. 581–588, May 1992.

22 L. Zhong, M. F. Rahman, W. Y. Hu, and K. W. Lim, "Analysis of direct torque control in permanent magnet synchronous motor drives," *IEEE Trans. Power Electron.*, vol. 12, no. 3, pp. 528–536, 1997.

23 T. G. Habetler, F. Profumo, M. Pastorelli, and L. M. Tolbert, "Direct torque control of induction machines using space vector modulation," *IEEE Trans. Ind Appl.*, vol. 28, no. 5, pp. 1045–1053, Oct. 1992.

24 G. S. Buja and M. P. Kazmierkowski, "Direct torque control of PWM inverter-fed AC motors—a survey," *IEEE Trans. Ind. Electron.*, vol. 51, no. 4, pp. 744–757, Aug. 2004.

25 L. Tang, L. Zhong, M. F. Rahman, and Y. Hu, "A novel direct torque controlled interior permanent magnet synchronous machine drive with low ripple in flux and torque and fixed switching frequency," *IEEE Trans. Power Electron.*, vol. 19, no. 2, pp. 346–354, Mar. 2004.

26 J. Rodriguez *et al.*, "Predictive current control of a voltage source inverter," *IEEE Trans. Ind. Electron.*, vol. 54, no. 1, pp. 495–503, Feb. 2007.

27 S. Kouro, P. Cortes, R. Vargas, U. Ammann, and J. Rodriguez, "Model predictive control—a simple and powerful method to control power converters," *IEEE Trans. Ind. Electron.*, vol. 56, no. 6, pp. 1826–1838, Jun. 2009.

28 J. Rodriguez *et al.*, "Latest advances of model predictive control in electrical drives—part I: basic concepts and advanced strategies," *IEEE Trans. Power Electron.*, vol. 37, no. 4, pp. 3927–3942, Apr. 2022.

29 J. Rodriguez *et al.*, "Latest advances of model predictive control in electrical drives—part II: applications and benchmarking with classical control methods," *IEEE Trans. Power Electron.*, vol. 37, no. 5, pp. 5047–5061, May 2022.

30 J. X. Shen, "Sensorless control of permanent magnet brushless drives," Ph.D. thesis, University of Sheffield, UK, 2003.

31 Y. F. Shi, Z. Q. Zhu, and D. Howe, "Torque-speed characteristics of interior-magnet machines in brushless ac and dc modes, with particular reference to their flux-weakening performance," *CES/IEEE 5th Int. Power Elect. Motion Control Conf.*, vol. 3, pp. 1–5, Aug. 2006.

32 K. Rajashekara, A. Kawamura, and K. Matsuse, *Sensorless Control of AC Motors*. New York, NY, USA: IEEE Press, 1996.